Applied Surface Science 263 (2012) 608–612

Contents lists available at SciVerse ScienceDirect

Applied Surface Science

journal homepage: www.elsevier.com/locate/apsusc

Improved corrosion resistance on biodegradable magnesium by zinc and aluminum ion implantation

Ruizhen Xu, Xiongbo Yang, Kai Wong Suen, Guosong Wu, Penghui Li, Paul K. Chu*

Department of Physics and Materials Science, City University of Hong Kong, Hong Kong, Hong Kong, China

ARTICLE INFO

Article history:
Received 20 July 2012
Received in revised form
20 September 2012
Accepted 22 September 2012
Available online 29 September 2012

Keywords:
Biomaterials
Magnesium
Ion implantation
Corrosion

ABSTRACT

Magnesium and its alloys have promising applications as biodegradable materials, and plasma ion implantation can enhance the corrosion resistance by modifying the surface composition. In this study, suitable amounts of zinc and aluminum are plasma-implanted into pure magnesium. The surface composition, phases, and chemical states are determined, and electrochemical tests and electrochemical impedance spectroscopy (EIS) are conducted to investigate the surface corrosion behavior and elucidate the mechanism. The corrosion resistance enhancement after ion implantation is believed to stem from the more compact oxide film composed of magnesium oxide and aluminum oxide as well as the appearance of the β-$Mg_{17}Al_{12}$ phase.

1. Introduction

In spite of unique mechanical properties, biodegradable characteristics, and good biocompatibility [1,2], magnesium and its alloys suffer from fast surface corrosion which must be addressed in real applications. Plasma immersion ion implantation (PIII) is an effective and efficient surface treatment technique [3–5]. In addition to its non-line-of-sight advantage, the process can be readily controlled by adjusting the plasma density, pulse width, and applied voltage [5]. Ion implantation of metallic elements into magnesium and its alloys has been suggested to modify the surface composition in an attempt to enhance the corrosion resistance and mechanical properties. For example, compact surface oxide films can be formed by Ce [6,7], Ti [7,8], Al [9,10], and Y [11,12] ion implantation into magnesium alloys to promote the corrosion resistance. The better mechanical properties and corrosion resistance introduced by Al [9] ion implantation is due to the increased second phase of β-$Mg_{17}Al_{12}$, whereas the dense MgO layer and alloy phase of Ta_2Al lead to better corrosion resistance after Ta [13] ion implantation. On the other hand, after Zn [14,15] ion implantation, the corrosion resistance is lower on account of the galvanic effect, but the surface hardness and modulus are improved. Cr [16] ion implantation results in a higher corrosion rate for the same reason as Zn, but subsequent O ion implantation retards corrosion by forming a surface oxide layer [17]. Owing to natural degradation of magnesium, the implanted metallic species can be released into body fluids and tissues causing deleterious effects and the type and amount of implanted elements must be carefully chosen to obtain the optimal corrosion resistance and biocompatibility.

Aluminum and zinc are popular alloying elements in commercial magnesium alloys and influence the mechanical, physical, and chemical properties of the materials. Aluminum can significantly improve the tensile strength *via* the formation of the β-$Mg_{17}Al_{12}$ phase. Zn plays a similar role as Al and can hinder the movement of the recrystallized grain boundary to refine the microstructure [18]. Commercial magnesium alloys such as Mg–Al–Zn alloys (AZ31 and AZ91) have in fact been suggested for biomedical applications [2,19–21]. Zinc is biologically benign being a necessary mineral and component of many proteins and nucleic acid and can accelerate cell metabolism [22]. However, a high aluminum concentration is harmful to neurons and osteoblasts and may be linked to dementia and Alzheimer's disease [23]. Aluminum also inhibits the phosphorylation process and ATP synthesis subsequently reducing the intracellular energy reserve [24]. Hence, the amount of Al released from the biodegradable Mg alloys must be carefully controlled. If the surface of magnesium can be alloying like the AZ alloy, it can hopefully enhance the corrosion resistance but with a lower dose of aluminum and zinc.

In this work, pure magnesium is implanted with zinc and subsequently aluminum. Since the mechanical characteristics after Zn or Al ion implantation is well known, this work mainly focuses on the corrosion behavior and corrosion mechanism. As a comparison, surface corrosion on pure magnesium, AZ31, AZ91 and implanted Mg is investigated systematically in simulated body fluids. To

* Corresponding author.
E-mail address: paul.chu@cityu.edu.hk (P.K. Chu).

0169-4332/$ – see front matter © 2012 Elsevier B.V. All rights reserved.
http://dx.doi.org/10.1016/j.apsusc.2012.09.116

understand the corrosion process and mechanism, a corrosion model is proposed based on the experimental data.

2. Experimental details

Three types of magnesium materials, as-cast pure magnesium blocks (99.95% pure; 10 mm × 10 mm × 5 mm), AZ31 blocks (Mg with 3 wt% Al and 1 wt% Zn; 10 mm × 10 mm × 5 mm), and AZ91 blocks (Mg with 9 wt% Al and 1 wt% Zn; 10 mm × 10 mm × 5 mm) were mechanically ground by up to #4000 water proof diamond paper and ultrasonically cleaned in ethanol. The pure magnesium blocks were implanted with zinc for 30 min at a terminal voltage of 15 kV and then aluminum for 120 min at the same voltage on the HEMII-80 ion implanter manufactured by Plasma Technology Ltd. The base pressure in the vacuum chamber was 10^{-4} Pa.

The Mg, Zn, and Al depth profiles were acquired by X-ray photoelectron spectroscopy (XPS) on a Physical Electronics PHI 5802. Al K_α irradiation was employed to determine the chemical states and the estimated sputtering rate was 6.2 nm/min. The phase constituents in the AZ91 and implanted sample were determined by X-ray diffraction (XRD, Rigaku SmartLab).

To evaluate the corrosion morphology, the implanted magnesium and pure magnesium samples were immersed in the simulated body fluid (SBF) for 3 h. The SBF was prepared with deionized water. The concentrations (mmol/l) of the various ions in the SBF were: 142.0 Na^+, 5.0 K^+, 1.5 Mg^{2+}, 2.5 Ca^{2+}, 147.8 Cl^-, 4.2 HCO^{3-}, 1.0 $HPO_4{}^{3-}$, 0.5 $SO_4{}^{2-}$. 1 mol/l HCl solution was pipette to adjust the pH to 7.25 at 37 °C. The temperature of SBF was kept at 37 ± 0.5 °C in a water bath. The samples after immersion were fully rinsed with de-ionized water and dried. The morphology and microstructure of the corroded surfaces were examined by using scanning electron microscopy (SEM, FEI/Philips XL30 Esem-FEG).

The electrochemical corrosion behavior of the implanted sample, pure magnesium, AZ31, and AZ91 were studied using a Zennium electrochemical workstation. The electrochemical tests were carried out in SBF using a three-electrode cell with the sample serving as the working electrode, calomel electrode as the reference electrode, and platinum sheet as the counter electrode. Potentiodynamic polarization tests were performed at a scanning rate 1 mV s^{-1}. Since rapid corrosion took place when the sample was soaked in SBF, potential scanning commenced as soon as the sample was exposed to the solution. The impedance data were recorded from 100 kHz to 100 mHz with a 10 mV sinusoidal perturbing signal. Equivalent circuits (EC) were proposed to analyze the obtained EIS spectra and the EIS spectra were fitted using the ZSimpWin software. All the electrochemical tests were performed at the ambient temperature 37 ± 0.5 °C.

3. Results and discussion

The XPS depth profiles obtained from the implanted sample depicted in Fig. 1 confirm that Zn and Al have been implanted. The Mg concentration increases steadily whereas the O signal decreases quickly in the near surface and then reaches to a terrace. Subsequently, the Mg concentration reaches around 100% and the O concentration drops to zero. The Al concentration is more than 10% in the beginning and then decreases gradually to zero. The distribution of Zn is Gaussian like. It is increasing slowly near the surface, reaching a peak concentration of about 17%, and dropping steadily to zero in the bulk.

The ion implant fluence of the HEMII-80 is calculated according to the following formula [25]:

$$D\left(\frac{\text{ions}}{\text{cm}^2}\right) = k\frac{I_\text{m}\cdot\tau\cdot n}{e\cdot S\cdot\overline{n_0}}, \quad (1)$$

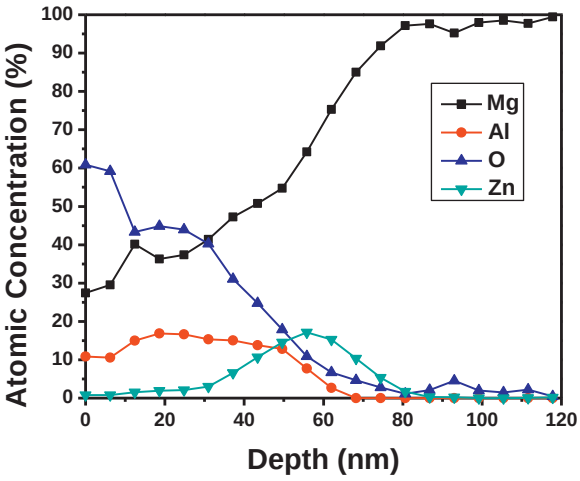

Fig. 1. XPS depth profiles obtained from the implanted sample.

where k is an empirical coefficient usually between 0.30 and 0.35, I_m is the average current, τ is the pulse width being 1 ms, n is the pulse number, e is the electron charge, S is ion beam area, and $\overline{n_0}$ is the average charge state number. Taking the average charge state number of Zn as being +1.4 [26], the ion implant fluence after implantation for 30 min is about 8.7×10^{16} ions cm^{-2}. Since the average state number of Al is +1.7, the ion implant fluence after implantation for 120 min is about 3.6×10^{17} ions cm^{-2}.

Fig. 2 presents the XPS spectra of the Mg 1s, Al 2p and Zn $2p_{3/2}$ peaks in the implanted sample revealing the changes in the chemical states with sputtering depth. As shown in Fig. 2a and b, the trends of Mg and Al are similar. With increasing sputtering time, the binding energies shift to lower values, suggested transformation from oxide to metallic states [27]. As shown in Fig. 2c, the Zn pattern changes from being flat to Gaussian. It implies that Zn exists mainly in a deeper region in the metallic state but there is hardly any Zn in the outermost surface. This is in good agreement with the concentration distribution of Zn in Fig. 1. The XPS results indicate that the surface film consists of roughly three different layers: an outer layer consisting mainly of magnesium oxide and aluminum oxide, an intermediate alloyed layer with magnesium, aluminum, and zinc, as well as an inner layer rich in magnesium.

To better understand the phase composition of the implanted sample, its diffraction pattern is compared to that of AZ91 before and after immersion in Fig. 3. Before immersion, the AZ91 and implanted sample exhibit diffraction peaks corresponding to the Mg phase. The individual diffraction peak of intermetallic β-$Mg_{17}Al_{12}$ phase is detected from the AZ91 magnesium alloy [8]. In previous studies [8,10,13,28–30], metal ion implantation yielded hybrid effects of ion irradiation and deposition forming an ion mixed layer. The diffraction pattern shows the appearance of the β-$Mg_{17}Al_{12}$ phase after ion implantation. Another diffraction peak of $MgAl_2O_4$ is observed from the implanted sample [10]. Because of the low ion implant fluences, the intensities of the β phase and oxide phase are relatively weak in the implanted sample. The data also indicate a three-layered surface film similar to that disclosed by XPS. After immersion in SBF for 3 h, the XRD patterns of the corroded samples are similar to those of the fresh samples, and no new phase can be detected. The results indicate that the corrosion products on the surface have an amorphous nature.

As shown in Fig. 4a, the scratches from the mechanical polishing can be seen from the pure Mg. However, in Fig. 4b, pits are formed from ions implantation on the scratches. After immersion in SBF for 3 h, the surface of Mg, in Fig. 4c, is covered by a uniform

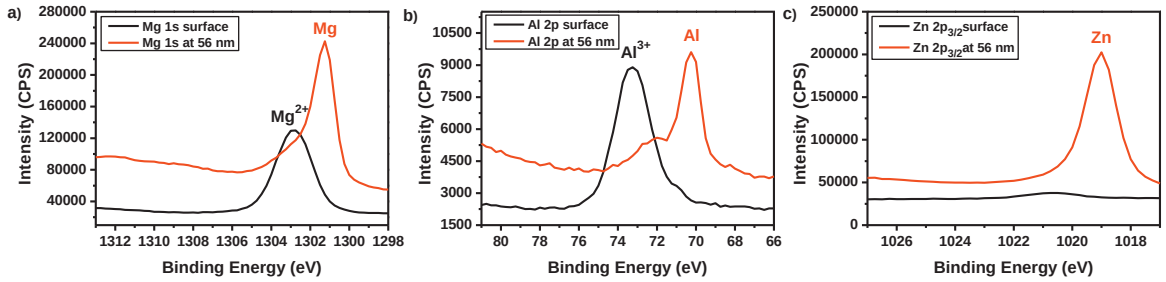

Fig. 2. XPS spectra of the implanted sample *versus* sputtering depth: (a) Mg 1s, (b) Al 2p, and (c) Zn $2p_{3/2}$.

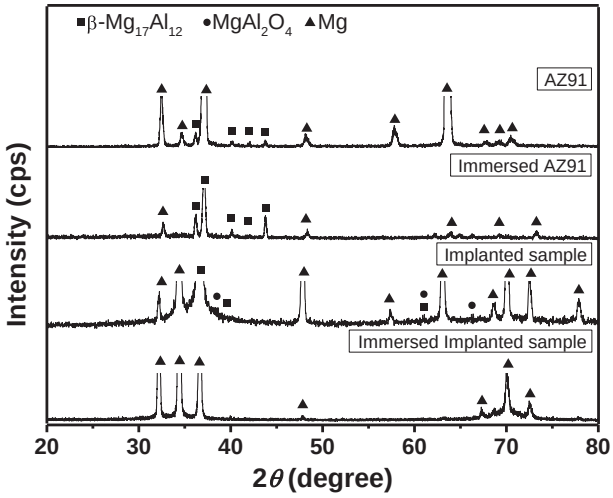

Fig. 3. XRD patterns of AZ91 and implanted samples.

corrosion product. The Mg surface is severely corroded as manifested by block-like products and cracks. On account of the inherently high chemical activity, the surfaces of Mg and its alloys form oxide layers upon exposure to air. This oxide film comprises mainly MgO which is converted into $Mg(OH)_2$ in an aqueous solution by the following reaction [31]:

$$MgO + H_2O \rightarrow Mg(OH)_2. \quad (2)$$

This layer is not compact and easily penetrated by Cl^- ions in the solution forming $MgCl_2$ [32] leading to severe corrosion in SBF.

Then after ion implantation, only small pits and cracks can be found by SEM in Fig. 4d. Previous studies point out that ion bombardment produces a dense oxide layer that yields enhanced corrosion resistance in SBF [8,9]. It is believed that the compact oxide surface may be an important factor in the improved electrochemical stability of the implanted sample. Moreover, the new β-$Mg_{17}Al_{12}$ phase may act as a barrier to impede corrosion. However, when defects exist in the passivation layer, some pits and cracks appear. The pitting corrosion arises for two reasons. First of all, the oxide film is not perfect and the inhomogeneous composition and microstructure produces vulnerable regions for pitting corrosion similar to Eq. (2). Secondly, because of the galvanic effects resulting from the inhomogeneous microstructure, the microanode has the α phase and the microcathode has the β phase similar to the AZ alloys [31]. Evolution of hydrogen makes it difficult for the corrosion products to precipitate at the microcathode and it gathers at the microanode. This process contributes to pitting corrosion *via* the following reaction:

$$M + nH_2O \rightarrow M(OH)_n + \frac{n}{2}H_2, \quad (3)$$

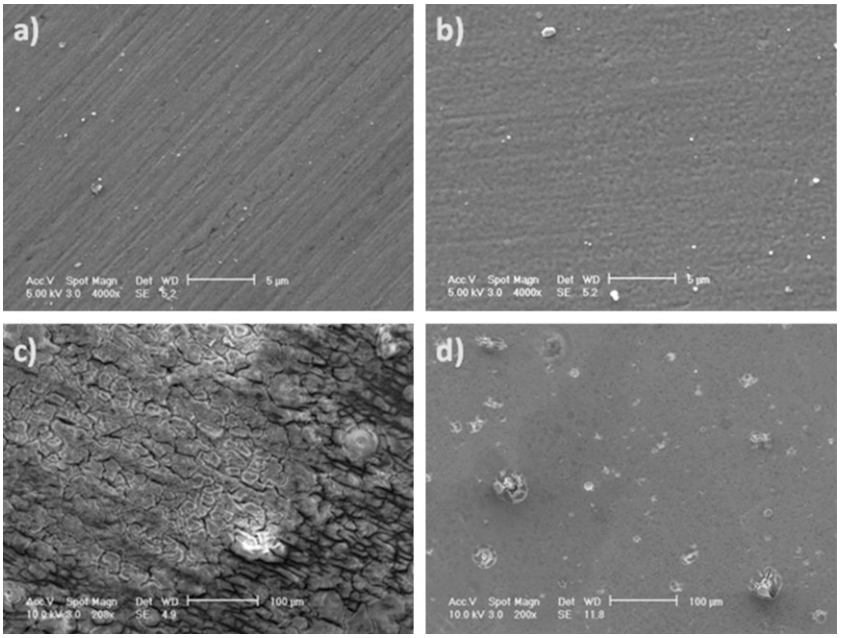

Fig. 4. Surface morphology of samples: (a) pure magnesium before immersed in SBF, (b) implanted sample before immersed in SBF, (c) pure magnesium after immersed in SBF, (d) implanted sample after immersed in SBF.

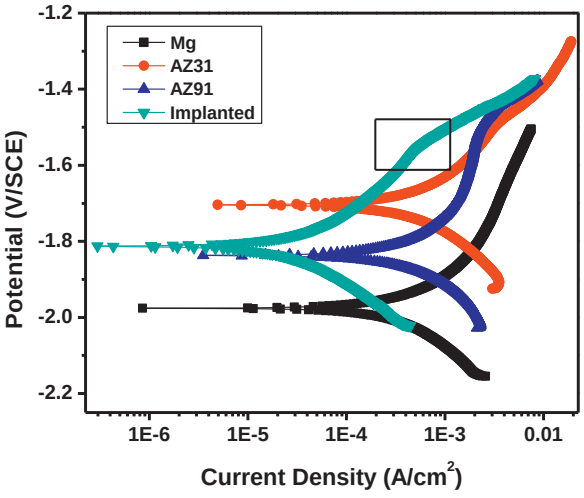

Fig. 5. Potentiodynamic polarization curves of different samples.

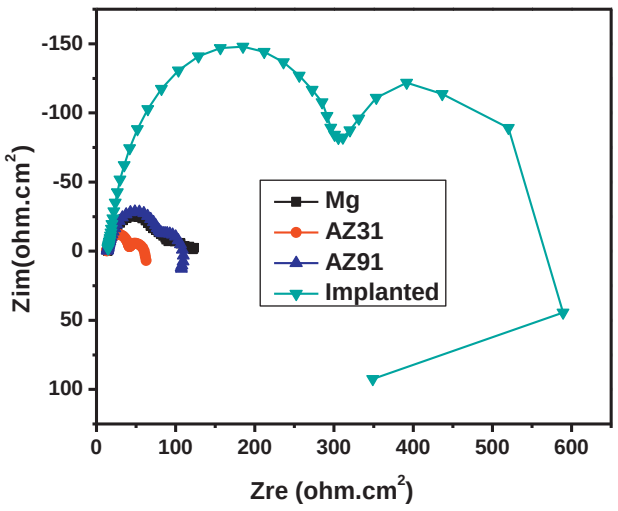

Fig. 6. Electrochemical impedance spectra of different samples.

where M represents Mg, Al, or Zn and $n = 2$ or 3 depending on the kind of alloying element dissolved [31,33].

Potentiodynamic polarization curves provide useful information of the corrosion behavior and corrosion rate. The potentiodynamic polarization curves of the four samples in the SBF are depicted in Fig. 5. Pure magnesium exhibits the most negative corrosion potential (−1.976 V). The implanted sample (−1.8125 V) has a similar corrosion potential as AZ91 (−1.8368 V). AZ31 shows the highest corrosion potential (−1.7038 V). The results indicate that the implanted sample has higher corrosion potential than pure magnesium over 160 mV. After ion implantation, the corrosion potential of pure magnesium shifts to the AZ alloys. The corrosion resistance is closely related to the corrosion current density. The higher the corrosion resistance, the lower is the corrosion current density. The corrosion current densities of Mg, AZ91, and AZ31 are 3.59×10^{-4} A/cm^2, 4.61×10^{-4} A/cm^2, and 4.59×10^{-4} A/cm^2, respectively. The corrosion current density of the implanted sample (2.27×10^{-5} A/cm^2) is an order of magnitude smaller than that of the other three samples. It implies that the degradation rate of magnesium is indeed retarded by dual ions implantation. It is noted that an obvious passivation region is present in the anodic polarization curve of the implanted sample, which has a similar passivation behavior as the AZ31 and AZ91 magnesium alloys. After dual ion implantation, its corrosion potential is lower than that of AZ31 but higher than that of AZ91 while its corrosion current density is lower than that of AZ31 and AZ91. The corrosion resistance of implanted sample is improved.

The electrochemical behavior of the samples is investigated by electrochemical impedance spectroscopy (EIS) and Fig. 6 exhibits the EIS curves obtained from the four samples in SBF. The diameters of the capacitive loops represent the corrosion resistance [34] and so the enlarged capacitive loop of the implanted sample indicates higher corrosion resistance. As Mg, AZ31, and AZ91 have similar diameters in the capacitive loops, they have similar corrosion resistance. The results show good agreement with those of polarization.

The spectrum acquired from the implanted sample is characterized by three distinct loops: capacitive in the high frequency range, capacitive in the intermediate frequency range, and pseudoinductive in the low frequency range. The AZ31 and AZ91 samples have similar time constants as the implanted sample. The capacitive loops are often attributed to charge transfer, film effects, as well as mass transfer in the corrosion product layer. The pseudoinductive loop is associated with the existence of relaxation processes involving absorbed species on the vulnerable regions [35] and reflects the pitting corrosion mode [36].

When a small amplitude excitation signal is applied to the system, the response depends on the electrode kinetics which is quite complicated usually. It often contains several sub-processes including mass transfer, charge transfer, and so on. These sub-processes are in series or parallel with each other [37] and the combined impedance reflects all the sub-processes in the system. Taking the physical structure of the electrode system and its impedance response into account, the EC of the implanted sample and Mg alloys is proposed in Fig. 7. The EIS fitted results of the above three samples are presented in Table 1. R_s is the solution resistance between the reference and working electrode. Its value is determined by the conductivity of the test medium and cell geometry [31]. Since the reaction systems are similar, the values of solution resistance are similar in these three systems. C_f is one of the constant phase angle CPE components and represents the capacitance of the intact film on the surface. A larger value of C_f indicates that the dielectric constant of the surface film increases due to electrolyte penetration and/or film thickness reduction due to chemical dissolution. This suggests that the implanted sample has a more protective surface film. R_f is the relevant resistance named after pore or ionic conducting defect resistance. The implanted sample shows a larger R_f implying good corrosion resistance on the surface film. C_{dl}, another CPE component, denotes the capacitance of the interface electric double layer in the vulnerable regions exposed to electrolyte penetration. The variation in C_{dl} should be attributed to the deterioration of the surface film resulting in a larger area fraction of the vulnerable regions. After immersion in SBF, these three samples show pitting corrosion. Moreover, the corroded areas on the AZ alloys are larger than those on the implanted sample. This result is consistent with the variations of C_{dl}. The Faraday charge transfer resistance, R_t, is related to the electrochemical reaction in the same region. The higher the charge transfer resistance, the lower is the corrosion rate. Compared to AZ31 and AZ91, the charge transfer resistance is higher, meaning that the implanted sample

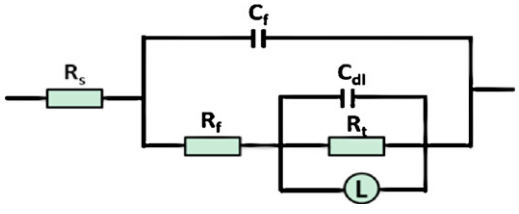

Fig. 7. Equivalent circuit (EC) for analysis of EIS spectra.

Table 1
Fitted results of EIS spectra.

Sample	R_s (Ω cm^2)	C_f (10^{-6} F cm^{-2})	m	R_f (Ω cm^2)	C_{dl} (10^{-6} F cm^{-2})	n	R_t (Ω cm^2)
AZ31	13.3	6969	0.7915	20.92	24.63	0.8745	28.56
AZ91	13.22	3410	0.4596	60.71	20.95	0.9344	51.4
Implanted	13.64	149.5	0.6238	610.4	2.942	1	181.8

has a smaller corrosion rate. Here, bigger values of R_t and R_f also correspond to smaller C_f and C_{dl}, respectively. In addition, L expresses the inductance and m and n are indices of the dispersion effect of the CPE components, C_f and C_{dl}, respectively representing deviations from the ideal capacitance because of the inhomogeneity and roughness of the electrode on the microscale. The values of m and n are in the range between 0 and 1 and obviously, the values are within this range.

Considering that the spectral shape before and after ion implantation is different, the corrosion mechanisms are different. With regard to Mg, the EC is proposed to be $R_s(C_fR_f)(C_{dl}R_t)$. This result reveals that the corrosion mode of Mg is general corrosion.

4. Conclusion

Zn and Al are implanted into pure magnesium at 15 kV for 0.5 and 2 h, respectively. The surface and chemical composition with depth and the phases in the implanted sample are determined. A three-layer surface film comprising an outer layer of magnesium oxide/aluminum oxide, a middle layer alloyed with metallic Zn, Al and Mg, and an inner layer rich in metallic Mg is formed. Immersion tests in simulated body fluids reveal better corrosion resistance on the implanted sample and pitting corrosion mode. Further investigation by electrochemical tests (polarization and EIS) confirms the immersion results and reveals the corrosion mechanism. The corrosion resistance enhancement observed from the implanted sample stems from the more compact hybrid oxide film as well as formation of the β-$Mg_{17}Al_{12}$ phase. Pitting corrosion on the implanted sample is a consequence of the inhomogeneous oxide film.

Acknowledgments

This study was supported by Hong Kong Research Grants Council (RGC) General Research Funds (GRF) no. CityU 112510.

References

[1] G.L. Song, A. Atrens, Advanced Engineering Materials 5 (2003) 837–858.
[2] F. Witte, V. Kaese, H. Haferkamp, E. Switzer, A. Meyer-Lindenberg, C.J. Wirth, H. Windhagen, Biomaterials 26 (2005) 3557–3563.
[3] J.R. Conrad, J.L. Radtke, R.A. Dodd, F.J. Worzala, N.C. Tran, Journal of Applied Physics 62 (1987) 4591–4596.
[4] P.K. Chu, B.Y. Tang, Y.C. Cheng, P.K. Ko, Review of Scientific Instruments 68 (1997) 1866–1874.
[5] P.K. Chu, J.Y. Chen, L.P. Wang, N. Huang, Materials Science and Engineering: R: Reports 36 (2002) 143–206.
[6] X.M. Wang, X.Q. Zeng, S.S. Yao, G.S. Wu, Y.J. Lai, Materials Characterization 59 (2008) 618–623.
[7] F. Chen, H. Zhou, S. Cai, F.X. Lv, C.M. Li, Rare Metals 26 (2007) 142–146.
[8] C.G. Liu, Y.C. Xin, X.B. Tian, J. Zhao, P.K. Chu, Journal of Vacuum Science and Technology A 25 (2007) 334–339.
[9] C.L. Liu, Y.C. Xin, X.B. Tian, P.K. Chu, Thin Solid Films 516 (2007) 422–427.
[10] M.K. Lei, P. Li, H.G. Yang, X.M. Zhu, Surface and Coatings Technology 201 (2007) 5182–5185.
[11] X.M. Wang, X.Q. Zeng, G.S. Wu, S.S. Yao, Applied Surface Science 253 (2006) 2437–2442.
[12] X.M. Wang, X.Q. Zeng, G.S. Wu, S.S. Yao, Y.J. Lai, Applied Surface Science 253 (2007) 3574–3580.
[13] X.M. Wang, X.Q. Zeng, G.S. Wu, S.S. Yao, Y.J. Lai, Journal of Alloys Compound 437 (2007) 87–92.
[14] G.S. Wu, L. Gong, K. Feng, S.L. Wu, Y. Zhao, P.K. Chu, Materials Letters 65 (2011) 661–663.
[15] Y.Z. Wan, G.Y. Xiong, H.L. Luo, F. He, Y. Huang, Y.L. Wang, Applied Surface Science 254 (2008) 5514–5516.
[16] R.Z. Xu, G.S. Wu, X.B. Yang, T. Hu, Q.Y. Lu, P.K. Chu, Materials Letters 65 (2011) 2171–2173.
[17] R.Z. Xu, G.S. Wu, X.B. Yang, X.M. Zhang, Z.W. Wu, G.Y. Sun, G.Y. Li, P.K. Chu, Applied Surface Science 258 (2012) 8273–8278.
[18] Y.L. Cheng, T.W. Qin, H.M. Wang, Z. Zhang, Transactions of Nonferrous Metals Society of China 19 (2009) 517–524.
[19] H.M. Wong, K.W.K. Yeung, K.O. Lam, V. Tam, P.K. Chu, K.D.K. Luk, K.M.C. Cheung, Biomaterials 31 (2010) 2084–2096.
[20] F. Witte, N. Hort, C. Vogt, S. Cohen, K.U. Kainer, R. Willumeit, F. Feyerabend, Current Opinion in Solid State and Materials Science 12 (2008) 63–72.
[21] G.D. Zhang, J.J. Huang, K. Yang, B.C. Zhang, H.J. Ai, Acta Metallurgica Sinica 43 (2007) 1186–1190.
[22] D.S. Yin, E.L. Zhang, S.Y. Zeng, Transactions of Nonferrous Metals Society of China 18 (2008) 763–768.
[23] S.X. Zhang, X.N. Zhang, C.L. Zhao, J.A. Li, Y. Song, C.Y. Xie, H.R. Tao, Y. Zhang, Y.H. He, Y. Jiang, Y.J. Bian, Acta Biomaterialia 6 (2010) 626–640.
[24] J.A. Helsen, H.J. Breme, Metals as Biomaterials, Wiley, Chichester, New York, 1998.
[25] K. Feng, G. Wu, T. Hu, Z. Li, X. Cai, P.K. Chu, Surface and Coatings Technology 206 (2012) 2914–2921.
[26] G.Y. Yushkov, A. Anders, E.M. Oks, I.G. Brown, Journal of Applied Physics 88 (2000) 5618–5622.
[27] M. Liu, S. Zanna, H. Ardelean, I. Frateur, P. Schmutz, G.L. Song, A. Atrens, P. Marcus, Corrosion Science 51 (2009) 1115–1127.
[28] X.M. Wang, X.Q. Zeng, G.S. Wu, S.S. Yao, Materials Letters 61 (2007) 968–970.
[29] X.B. Tian, C.B. Wei, S.Q. Yang, R.K.Y. Fu, P.K. Chu, Surface and Coatings Technology 198 (2005) 454–458.
[30] X.B. Tian, C.B. Wei, S.Q. Yang, R.K.Y. Fu, P.K. Chu, Nuclear Instruments and Methods B 242 (2006) 300–302.
[31] Y.J. Zhang, C.W. Yan, F.H. Wang, W.F. Li, Corrosion Science 47 (2005) 2816–2831.
[32] S.Z. Song, G.L. Song, Acta Physico-Chimica Sinica 22 (2006) 1222–1226.
[33] Y.C. Xin, C.L. Liu, X.M. Zhang, G.Y. Tang, X.B. Tian, P.K. Chu, Journal of Materials Research 22 (2007) 2004–2011.
[34] G.L. Song, A.L. Bowles, D.H. StJohn, Materials Science and Engineering: A Structural 366 (2004) 74–86.
[35] G. Song, A. Atrens, D. St John, X. Wu, J. Nairn, Corrosion Science 39 (1997) 1981–2004.
[36] Y.C. Xin, J. Jiang, K.F. Huo, G.Y. Tang, X.B. Tian, P.K. Chu, Journal of Biomedical Materials Research Part A 89A (2009) 717–726.
[37] C.N. Cao, Principles of Corrosive Electrochemistry, 2nd Ed., Chemical Industry Press, Beijing, 2004.